Temporal analysis of fringe projection profilometry using the continuous wavelet transform

Jesús Villa[a,*], Gamaliel Moreno[a], Ismael de la Rosa[a] and Rumen Ivanov[b].

[a]Unidad Académica de Ingeniería Eléctrica, Universidad Autónoma de Zacatecas, Campus Universitario UAZ Siglo XXI, Edificio E-14, Zacatecas 98107, México.
[b]Unidad Académica de Física, Universidad Autónoma de Zacatecas, Calz. Solidaridad, Esquina Paseo de la Bufa s/n, Campus Universitario II, Zacatecas 98060, México.

ARTICLE HISTORY
Compiled September 25, 2020

ABSTRACT

KEYWORDS
Sections; lists; figures; tables; mathematics; fonts; references; appendices

1. Introduction

2. Materials and methods

2.1. Generation of the fringe image sequence

Figure (1) shows the standard set-up for fringe projection profilometry. The digital projector illuminates the measurement volume with sinusoidal fringes which are perpendicular to the plane of the figure. In temporal methods the fringe pitch is changed over the time t, such that $t = 1, 2, \ldots, N$. With the proposed method, it is assumed that for $t = 1$ the fringe phase ranges in the interval (ω_1, ω_2), as shown in Figure (1). For subsequent fringe images the phase interval is increased such that $(\omega_1 t, \omega_2 t)$; therefore, the fringe frequency increases as t increases.
The intensity of the captured images is a function of the spatial coordinates (x, y) and time t, however, as the analysis is realized independently at each pixel, the spatial coordinates can be omitted. In this way, the intensity along time t at a given pixel can be modeled as

$$I(t) = I_0(t) + I_1(t)\cos\left[\Phi(t)\right], \tag{1}$$

where $\Phi(t) = \omega_t t + \phi$, being the angular temporal-frequency ω_t dependent on the pixel position such that $\omega_1 < \omega_t < \omega_2$.

CONTACT Jesús Villa. Email: jvillah@uaz.edu.mx

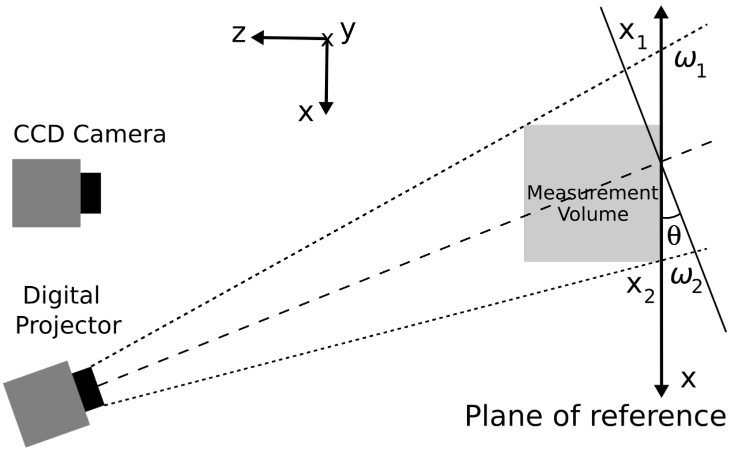

Figure 1. Schematic diagram of a basic system for the object's depth measurement based on fringe projection. The projected fringes and y-axis are perpendicular to the plane of the figure.

In the classical work by Huntley and Saldner [14], ω_1 and ω_2 are chosen such that $\omega_1 = -\pi$ and $\omega_2 = \pi$, which implies that $-\pi < \omega_t \leq 0$ in some pixels. Nevertheless, there is a main drawback using this approach: to determine the sign of ω_t and properly process pixels where $\omega_t \approx 0$ (*i.e.* pixels with zero modulation), it requires of at least two images per sample at time t. A particular interest in the present work is to choose an interval (ω_1, ω_2) for a proper number of cycles (periods) of the signal $I(t)$ such that $0 < \omega_t < \pi$. With this approach, the estimation of ω_t becomes more affordable for a wider variety of signal processing methods and thus try to increase accuracy and reduce the number of images.

To properly process the signal $I(t)$ with the method explained later, it is now analyzed in terms of the sampling and number of cycles. First, we define C and k as the number of cycles and the number of samples per cycle (temporal period), respectively. The frequency ω_t can now be defined in terms of C, k and N as

$$\omega_t = \frac{2\pi}{N}C = \frac{2\pi}{k}. \tag{2}$$

We can see that the sampling of $I(t)$ reaches the Nyquist limit when $C/N = 1/k = 1/2$, which means that $\omega_t = \pi$. In other words, the Nyquist limit is reached when the number of samples N represents two times the number of cycles, being $k = 2$.

Keeping in mind Equation (2), for a given N we can define the interval (ω_1, ω_2) in terms of cycles C. Conversely, for a given interval (ω_1, ω_2) in terms of cycles C we can determine the number of necessary samples (images) N such that $k \geq 2$. That is

$$k = \frac{N}{C} \geq 2. \tag{3}$$

2.2. Phase to height conversion

It is now deduced a formula to convert ω_t to real dimensions $z(x, y)$ of the measured object. The formula represents a first approximation to the desired measurement. Considering the optical set-up shown in Figure (1), it is well known that an approximation to the captured intensity by the CCD camera can be modeled as

$$I(x, y) = I_0(x, y) + I_1(x, y) \cos\left(2\pi f[x \cos\theta + z(x, y) \sin\theta]\right), \tag{4}$$

where f represents the frequency of the projected fringes, θ the angle between the optical axes of the CCD and the projector, and $z(x, y)$ the object's height distribution. The terms I_0 and I_1 represent the background illumination and the amplitude modulation, respectively. To model the fringe sequence along time t we use the angular spatial-frequency $\omega_s = 2\pi f$.

$$I(x, y, t) = I_0(x, y, t) + I_1(x, y, t) \cos\left(\omega_s t[x \cos\theta + z(x, y) \sin\theta]\right). \tag{5}$$

According to Figure (1), we can deduce that

$$\omega_1 < \omega_s[x \cos\theta + z(x, y) \sin\theta] < \omega_2. \tag{6}$$

Now, introducing the angular temporal-frequency $\omega_t = \omega_s[x \cos\theta + z(x, y) \sin\theta]$ and omitting the spatial coordinates, we rewrite the image-sequence model as

$$I(t) = I_0(t) + I_1(t) \cos\left(\omega_t t + \phi\right), \tag{7}$$

where ϕ is a phase-shift that depends on the spatial coordinates (x, y). According to the definition of ω_t, we deduce that

$$z = \frac{\frac{\omega_t}{\omega_s} - x \cos\theta}{\sin\theta}. \tag{8}$$

Of course, considering that x coordinate is such that $x_1 < x < x_2$ in the field of view, as depicted in Figure (1), then

$$\omega_s = \frac{\omega_2 - \omega_1}{x_2 - x_1}. \tag{9}$$

The formula (8) is valid if $x_2 - x_1$ and z are much smaller than the distance of the projector to the object under test.

2.3. The Continuous Wavelet Transform

Consider a signal as the represented in Equation (1). Then, its Continuous Wavelet Transform can be defined as

$$\mathcal{W}_{a,b}\{I(t)\} = \int_{-\infty}^{\infty} I(t)\psi^*\left(\frac{t-b}{a}\right) dt, \tag{10}$$

where ψ represents the mother wavelet and $*$ the complex conjugated. Note that $\mathcal{W}_{a,b}\{I(t)\}$ is a two-dimensional function of a and b, that represent the scale and shifting, respectively.

The proper choice of ψ depends on the particular problem. For the case of a cosine signal as (1), where the parameter to be estimated is the phase or frequency, the most convenient choice is the Gabor Wavelet, that can be defined as

$$\psi(t) = e^{-\frac{t^2}{2\sigma^2}} e^{i2\pi f_0 t}, \tag{11}$$

which represents a complex periodic function modulated by a Gaussian function, where f_0 and σ^2 represent the frequency and the variance, respectively. Figure (2) shows an example of a Gabor Wavelet.

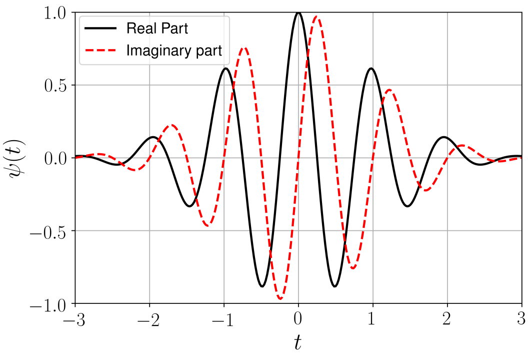

Figure 2. Example of a Gabor wavelet with $f_0 = \sigma^2 = 1$.

To estimate the phase or the frequency of $I(t)$, the ridge detection must be realized. The ridge represents the scales a for each b where $\|\mathcal{W}_{a,b}\|$ is maximum.

In order to simplify the following explanation about the method to estimate the frequency from the ridge detection, we set $f_0 = 1$. Also, we rewrite Equation (1) in complex form as

$$I(t) = I_0(t) + \frac{I_1(t)}{2} e^{i\Phi(t)} + \frac{I_1(t)}{2} e^{-i\Phi(t)}. \tag{12}$$

Assuming that $I_0(t)$ and $I_1(t)$ are constants, then

$$\begin{aligned} \mathcal{W}_{a,b}\{I(t)\} = I_0 &\int_{-\infty}^{\infty} e^{-\frac{1}{2\sigma^2}(\frac{t-b}{a})^2} e^{-i2\pi(\frac{t-b}{a})} dt \\ &+ \frac{I_1}{2} \int_{-\infty}^{\infty} e^{-\frac{1}{2\sigma^2}(\frac{t-b}{a})^2} e^{-i2\pi(\frac{t-b}{a})} e^{i\Phi(t)} dt \\ &+ \frac{I_1}{2} \int_{-\infty}^{\infty} e^{-\frac{1}{2\sigma^2}(\frac{t-b}{a})^2} e^{-i2\pi(\frac{t-b}{a})} e^{-i\Phi(t)} dt. \end{aligned} \tag{13}$$

Changing the variables $\nu = 1/a$ and $\tau = t-b$, and knowing that $\Phi(b+\tau) = \Phi(b) + \omega_t \tau$, where $\omega_t = \frac{2\pi}{k}$, then

$$
\begin{aligned}
\mathcal{W}_{a,b}\{I(t)\} = I_0 & \int_{-\infty}^{\infty} e^{-\pi(\frac{\nu\tau}{\sigma\sqrt{2\pi}})^2} e^{-i2\pi\nu\tau} d\tau \\
& + \frac{I_1}{2} e^{i\Phi(b)} \int_{-\infty}^{\infty} e^{-\pi(\frac{\nu\tau}{\sigma\sqrt{2\pi}})^2} e^{i\frac{2\pi}{k}\tau} e^{-i2\pi\nu\tau} d\tau \\
& + \frac{I_1}{2} e^{-i\Phi(b)} \int_{-\infty}^{\infty} e^{-\pi(\frac{\nu\tau}{\sigma\sqrt{2\pi}})^2} e^{-i\frac{2\pi}{k}\tau} e^{-i2\pi\nu\tau} d\tau.
\end{aligned}
\tag{14}
$$

The factor $e^{-i2\pi\nu\tau}$ at each term in Equation (14) represents the Fourier transform kernel, then, evaluating the three Fourier transforms using the modulation and similarity theorems, we obtain

$$
\begin{aligned}
\mathcal{W}_{a,b}\{I(t)\} &= a\sigma\sqrt{2\pi} I_0 e^{-2(\pi\sigma)^2} \\
&+ a\sigma\sqrt{2\pi}\frac{I_1}{2}\left[e^{i\Phi(b)} e^{-2(\pi\sigma)^2\left(1-\frac{a}{k}\right)^2} + e^{-i\Phi(b)} e^{-2(\pi\sigma)^2\left(1+\frac{a}{k}\right)^2}\right].
\end{aligned}
\tag{15}
$$

2.4. Ridge detection and frequency estimation

Consider the following one-dimensional function of scale a for a given shift b.

$$
S(a) = I_0 e^{-2(\pi\sigma)^2} + \frac{I_1}{2} e^{i\Phi(b)} e^{-2(\pi\sigma)^2\left(1-\frac{a}{k}\right)^2} + \frac{I_1}{2} e^{-i\Phi(b)} e^{-2(\pi\sigma)^2\left(1+\frac{a}{k}\right)^2}. \tag{16}
$$

Note that $S(a)$ is obtained dividing Equation (15) by $a\sigma\sqrt{2\pi}$. It can be seen that first term in Equation (16) is a small constant, second term contains a Gaussian function with variance $k^2/(4\pi^2\sigma^2)$ and mean at $a = k$. Finally, third term contains a Gaussian function with variance $k^2/(4\pi^2\sigma^2)$ and mean at $a = -k$, therefore, as $k \geq 2$ and scales a must be such that $a > 0$, third term has no significant influence. For this reason the ridge detection (*i.e.* the scale $a_r = k$ for each b) can be well approximated estimating the mean of $\|S(a)\|$ for each b, given that

$$
\|S(a)\| \approx \frac{I_1}{2} e^{-2(\pi\sigma)^2\left(1-\frac{a}{k}\right)^2}. \tag{17}
$$

Figure (3) shows graphs of $\|S(a)\|$ for different values of σ^2 and k. Note that the variance of $\|S(a)\|$ increases as k increases.

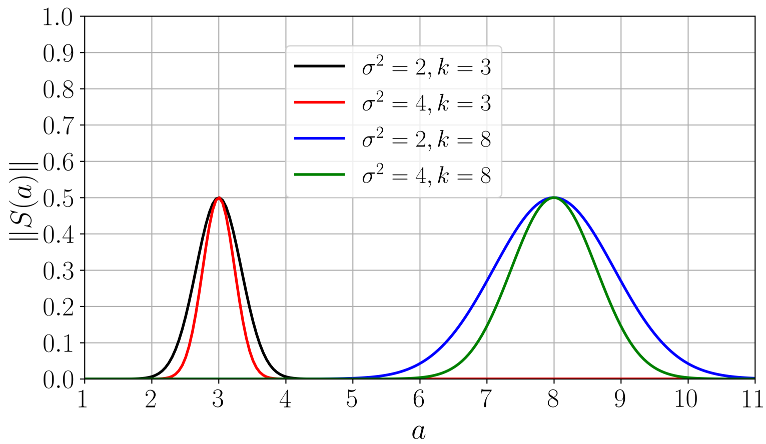

Figure 3. Simulated graphs of $\|S(a)\|$ with $I_0 = I_1 = 1$.

Figures (4) and (5) show examples of simulated signals $I(t)$ and their corresponding $\|\mathcal{W}_{a,b}\|$, using $\sigma^2 = 2$ and $\sigma^2 = 4$.

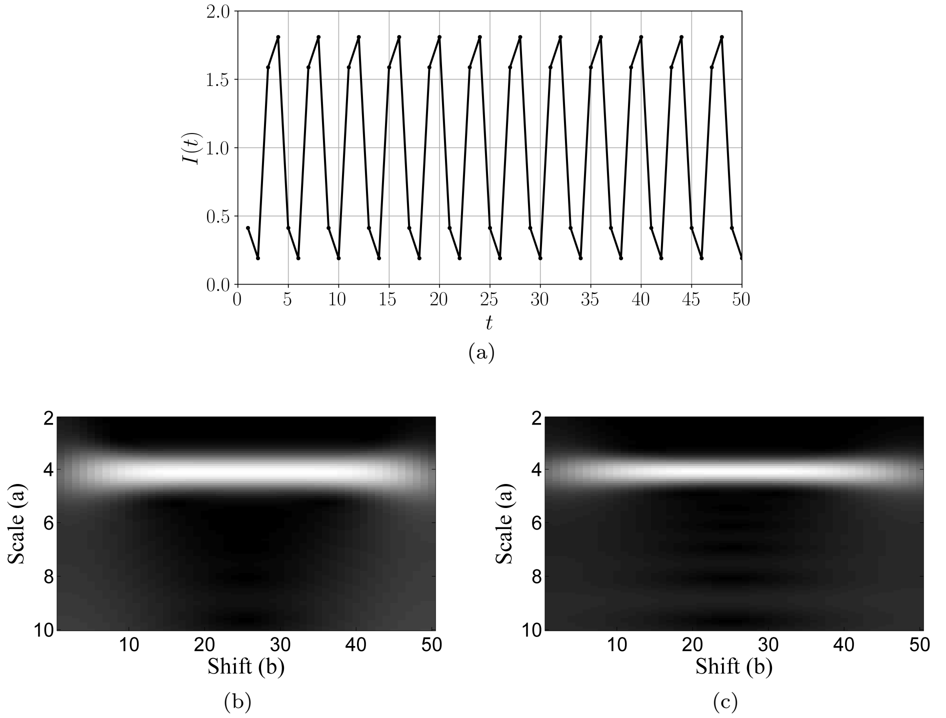

Figure 4. (a) Simulated signal $I(t)$ with $k = 4$, using 50 samples. (b) Gray level codification of $\|\mathcal{W}_{a,b}\|$ with $\sigma^2 = 2$. (c) Gray level codification of $\|\mathcal{W}_{a,b}\|$ with $\sigma^2 = 4$. To compute the CWT, we used a set of 100 scales ranging in the interval $[2, 10]$.

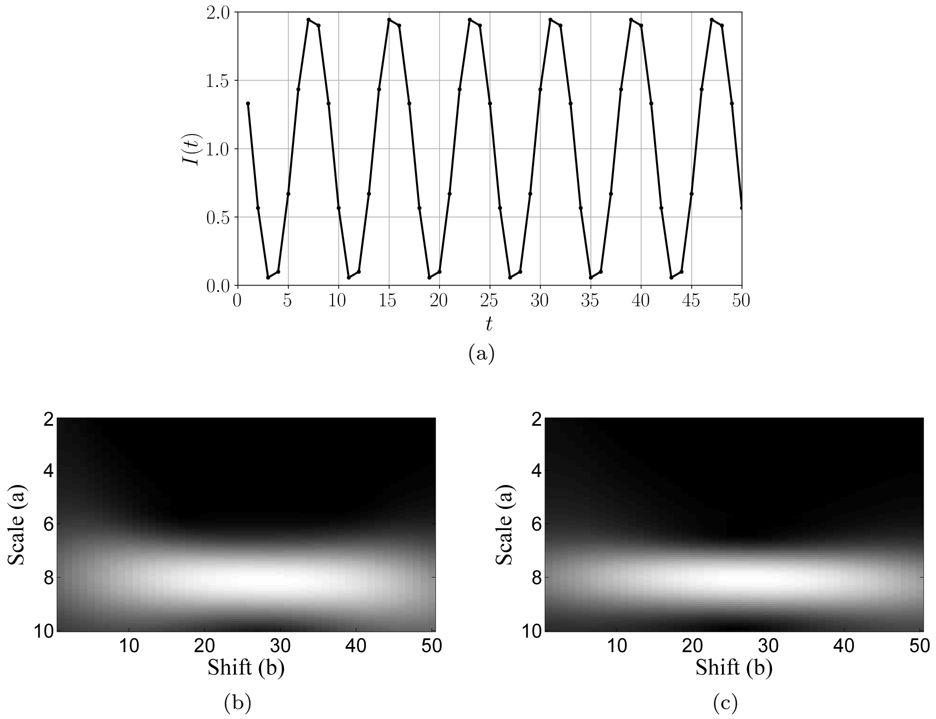

Figure 5. (a) Simulated signal $I(t)$ with $k = 8$, using 50 samples. (b) Gray level codification of $\|\mathcal{W}_{a,b}\|$ with $\sigma^2 = 2$. (c) Gray level codification of $\|\mathcal{W}_{a,b}\|$ with $\sigma^2 = 4$. To compute the CWT, we used a set of 100 scales ranging in the interval $[2, 10]$.

We now address the issue of estimating a_r from Equation (16). Such a task can be accomplished taking advantage of the form of $\|S(a)\|$. Therefore, this may be carried out computing the mean of $\|S(a)\|$. Despite this strategy may be feasible in ideal conditions, unfortunately, spurious information like noise may introduce large errors. Hence, noise must be reduced in the whole domain of $\|S(a)\|$. This may be achieved computing a power of $\|S(a)\|$, that is

$$\|S(a)\|^p \approx \left(\frac{I_1}{2}\right)^p e^{-2p(\pi\sigma)^2\left(1-\frac{a}{k}\right)^2}, \qquad p > 1. \tag{18}$$

There are two main advantages using this approach: first, spurious information gets strongly attenuated with respect to the Gaussian function. Second, the Gaussian function gets narrower, which is an outcome that constitutes an improvement in the estimations with low-frequency signals (large k). In this way, considering a set of N_a scales $\{a_n\}$ shuch that $a_n \in [a_1, a_2]$ and $n = 1, 2, \ldots, N_a$, then, the mean of $\|S(a)\|^p$ (the ridge a_r) at a given b can be estimated with

$$a_r = \frac{\sum_{n=1}^{N_a} \|S(a_n)\|^p a_n}{\sum_{n=1}^{N_a} \|S(a_n)\|^p}. \tag{19}$$

The value of k, which defines the spatial angular frequency $\omega_t = 2\pi/k$, is then estimated computing the mean of scales a_r of all shifts b.

2.5. Parameter selection for frequency estimation

For an accurate estimation of k, the parameter selection plays a crucial role. As previously described, the temporal frequency interval $\omega_1 < \omega_t < \omega_2$ (*i.e.* the spatial fringe-phase-interval) can be defined in terms of samples per cycle such that $k \geq 2$. Although working near the Nyquist sampling is adequate for accurate estimations, care must be taken not to be at the limit to avoid aliasing that may cause large errors. On the other hand, working with large values of k causes a decrease in the precision of the estimates.

An adequate selection of f_0 and σ^2 depends on the signal to be processed. As $\omega_t > 0$, for simplicity we just select $f_0 = 1$. On the other hand, σ^2 has an influence on the accuracy in two main aspects: the number of samples (images) N and the sampling k. Due to the finite extension of $I(t)$, low-precision estimates of the ridge a_r may occur in the borders of the signal (see $\|\mathcal{W}_{a,b}\|$ in Figures (4) and (5)). Hence, care should be taken in selecting the parameter σ^2 when using few images. Also, as σ^2 and k determine the variance of $\|S(a)\|$, small values of σ^2 may cause a decrease in the precision of the estimates.

To select adequate values of ω_1 and ω_2 in terms of k and the number of samples N, the following numerical experiment was performed. With a set of values of k such that $k > 2$, a set of 500 signals $I(t)$ for each k were simulated according to the expression

$$I(t) = I_0 + I_1 \cos\left[\frac{2\pi}{k}t + \phi + n_\phi\right], \tag{20}$$

where we set $I_0 = I_1 = 1$ for simplicity, $\phi \in [0, 2\pi)$ is a phase constant randomly generated for each simulation, and n_ϕ is a Gaussian phase-noise with variance 0.1. For each k the mean absolute percentage error (MAPE) was computed:

$$M(k) = \frac{100}{N_e}\sum_{e=1}^{N_e}\left|\frac{k - \hat{k}_e}{k}\right|, \quad N_e = 500, \tag{21}$$

where $\hat{k}_e$ is the estimated k with the CWT.

Figure (6) shows the graphs of $M(k)$ for different values of N. In this case, we used a set of 50 values of k in the interval $[2.5, 5]$. In the experiment, $\sigma^2 = 1.75$ and $p = 4$ were the values that gave the best results using a set of $N_a = 20$ scales in the interval $[2, 6]$. Neither with the increase in the number of scales nor with the increase in the interval, were the results significantly improved.

We have found that keeping the parameters at values close to those of the previous experiment, the results provide the highest accuracy in most cases. Therefore, the recommended parameter values are shown in Table (1).

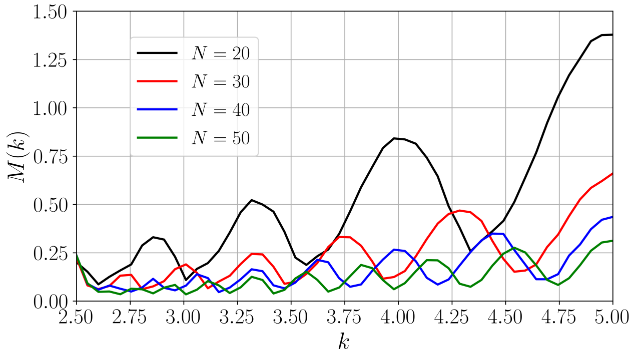

Figure 6. Graphs of $M(k)$ for different values of N.

Table 1. Recommended parameters values for frequency estimation using the CWT.

$\omega_1 = \frac{2\pi}{k_1}$	$\omega_2 = \frac{2\pi}{k_2}$	N	σ^2	f_0	a_n	N_a	p
$k_1 = 5$	$k_2 = 2.5$	$N \geq 20$	$[\frac{3}{2}, 2]$	1	$[2, 7]$	$N_a \geq 20$	4

3. Experimental results

3.1. Simulations and error analysis

In order to analyze the performance of the proposed method compared with a previously reported temporal technique, the following numerical experiments were realized. We have selected the representative method reported by Huntley *et al* [14], using the linear sequence. As known, to compute the phase value for a given t, the Huntley's method uses a phase-shifting algorithm that requires four phase-shifted fringe images; therefore, a full of $N_i = 4N$ images must be captured. On the other hand, the proposed method requires a full of $N_i = N$ images.

Figure (7) shows a 100×100 simulated depth distribution $z(x, y)$. In the same figure are shown the corresponding ω_t distribution (angular temporal-frequency) as depicted in the work by Huntley *et al*, and the ω_t distribution as proposed in this work.

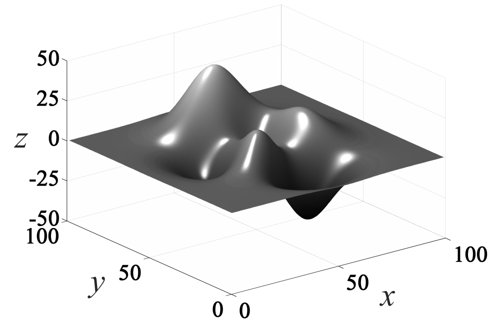

(a)

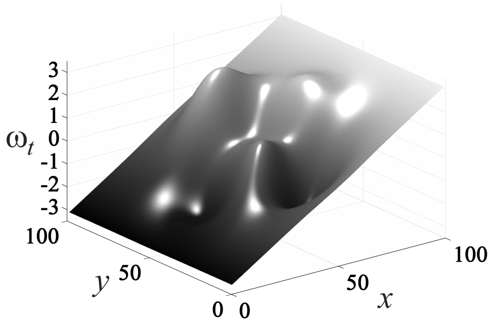

(b)

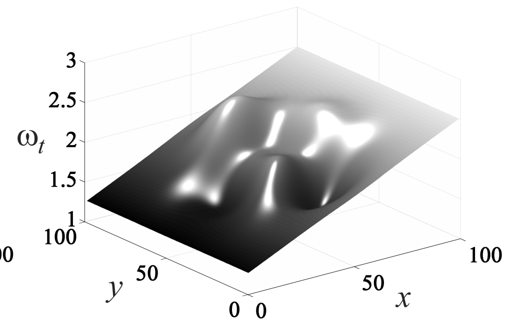

(c)

Figure 7. (a) Simulated $z(x, y)$ using an array of 100×100. Spatial fringe-phase ω_t (temporal angular-frequency) generated with $z(x, y)$: (b) $-\pi < \omega_t < \pi$ (Huntley). (c) $\frac{2\pi}{5} < \omega_t < \frac{2\pi}{2.5}$ (As proposed in this work).

To characterize the performance of the compared methods we used the Normalized Root Mean Square Error (NRMSE), which is computed with

$$\text{NRMSE} = \sqrt{\frac{\|\omega_t - \hat{\omega}_t\|^2}{\|\omega_t\|^2}}, \tag{22}$$

where ω_t and $\hat{\omega}_t$ represent the simulated and the estimated frequency, respectively. We have realized that using the spatial fringe-phase $-\pi < \omega_t < \pi$, as depicted in [14], the Huntley's method has a much lower performance than using the distribution $\frac{2\pi}{5} < \omega_t < \frac{2\pi}{2.5}$, therefore, we have compared both methods using the same spatial fringe-phase distribution $\frac{2\pi}{5} < \omega_t < \frac{2\pi}{2.5}$. Figure(8) shows such performance comparison for different N_i and noise levels.

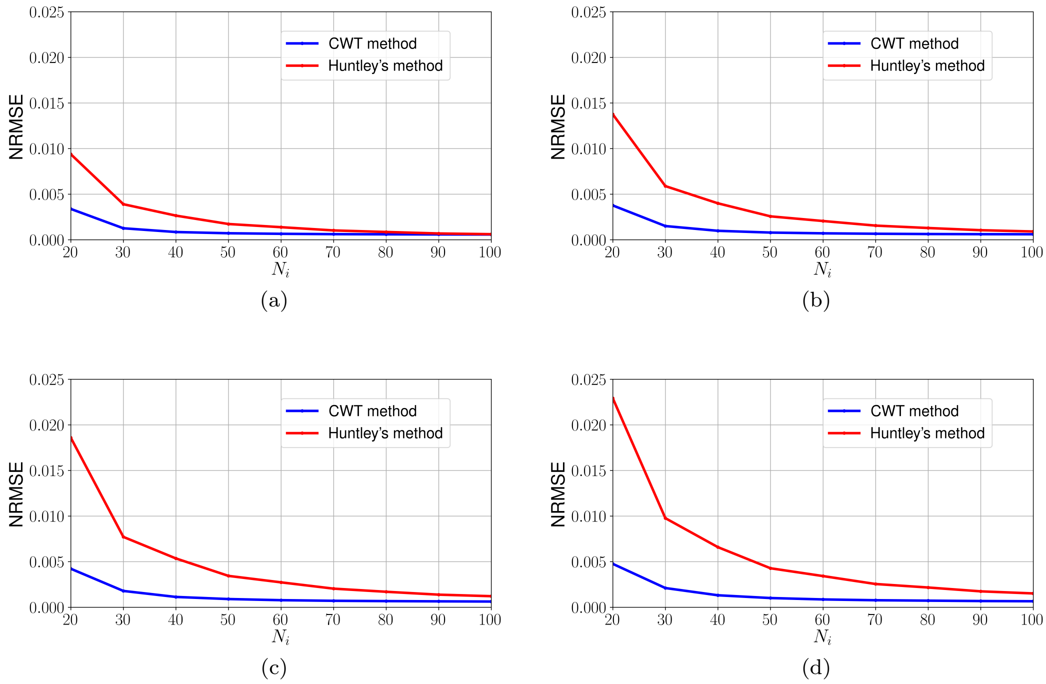

Figure 8. Comparison between the CWT method and the Huntley's method for different number of images and different variances of Gaussian phase-noise. Variance: (a) 0.04, (b) 0.06, (c) 0.08, (d) 0.10.

3.2. Application to real objects

4. Conclusions

Acknowledgements

We acknowledge to the Consejo Nacional de Ciencia y Tecnología (CONACYT) of México for the scholarship of Susana Burnes and the Retención grant (No. 2019-000010-01NACV-00020) of Gamaliel Moreno.

References

[1] Gasvik KJ. Optical Metrology, 3rd ed., John Wiley & Sons, 2002.
[2] Cloud G. Optical Methods of Engineering Analysis, Cambridge University Press, 1995.
[3] Sirohi S. Optical Methods of Measurement, Wholefield Techniques, Second Edition, CRC Press, 2009.
[4] Leach R. Optical Measurement of Surface Topography, Springer, 2011.
[5] Zhang S. Recent progresses on real-time 3D shape measurement using digital fringe projection techniques, Opt. Las. Eng. 2010; 48(2): 149–158.
[6] Kulkarni R and Rastogi P. Optical measurement techniques - A push for digitization, Opt. Las. Eng. 2016; 87: 1–17.
[7] Jeught SV and Dirckx JJ. Real-time structured light profilometry: a review. Opt. Las. Eng. 2016; 87: 18–31.
[8] Takeda M and Mutoh K. Fourier transform profilometry for the automatic measurement of 3-D object shapes. Appl. Opt. 1983; 22(24): 3977–3982.

[9] Li J, Su XY, and Guo LR. Improved Fourier transform profilometry for the automatic measurement of three-dimensional object shapes. Opt. Eng. 1990; 29(12): 1439–1444.
[10] Malacara D, Servín M and Malacara Z. Interferogram Analysis for Optical Testing, Second Edition, Taylor & Francis, 2005.
[11] Li D, Liu C, and Tian J. Telecentric 3D profilometry based on phase-shifting fringe projection. Opt. Exp. 2016; 22(26): 31826–31835.
[12] YePeng L, Guangliang D, ChaoRui Z, CanLin Z, ShuChun S, and Zhenkun L. An improved two-step phase-shifting profilometry. Optik 2016; 127(1): 288–291.
[13] Ayubi GA, Martino JM, Alonso JR, Fernandez A, Perciante CD, Ferrari JA Three-dimensional profiling with binary fringes using phase-shifting interferometry algorithms. Appl. Opt. 2011; 50(12): 147–154.
[14] Huntley JM and Saldner HO. Error-reduction methods for shape measurement by temporal phase unwrapping. J. Opt. Soc. Am. A 1997; 14(12): 3188–3196.
[15] Coggrave CR and Huntley JM. High-speed surface profilometer based on a spatial light modulator and pipeline image processor. Opt. Eng. 1999; 38(9): 1573–1581.
[16] Ng TW, Ang KT, and Argentini G. Temporal fringe pattern analysis with parallel computing. Appl. Opt. 2005; 44(33): 7125–7129.
[17] Quiroga JA and Gomez-Pedrero JA. Temporal phase evaluation by Fourier analysis of fringe patterns with spatial carrier. J. Mod. Opt. 2001; 48(14): 2129–2139.
[18] Villa J, Gomez-Pedrero JA, Quiroga JA. Synchronous detection technique for temporal fringe pattern analysis. Opt. Comm. 2001; 204: 75–81.
[19] Zou C, Huang L, Zhang M, Chen Q and Asundi A. Temporal phase unwrapping algorithms for fringe projection profilometry: A comparative review. Opt. Las. Eng. 2016; 85: 84–103.
[20] Servin M, Padilla M, Garnica G, Gonzalez A. Profilometry of three-dimensional discontinuous solids by combining two-steps temporal phase unwrapping, co-phased profilometry and phase-shifting interferometry. Opt. Las. Eng. 2016; 87: 75–82.
[21] Petković T, Donlić M. Temporal phase unwrapping using orthographic projection. Opt. Las. Eng. 2017; 90: 34–47.
[22] Tay CJ, Quan, Sun CW, He XY. Demodulation of a single interferogram based on continuous wavelet transform and phase derivative. Opt. Comm. 2007; 280: 327–336.
[23] Watkins LR. Phase recovery from fringe patterns using the continuous wavelet transform. Opt. Las. Eng. 2007; 45: 298–303.
[24] Watkins LR. Review of fringe pattern phase recovery using the 1-D and 2-D continuous wavelet transforms. Opt. Las. Eng. 2012; 50: 1015–1022.
[25] Gdeisat MA, Abid A, Burton DR, Lalor MJ, Lilley F, Moore C, Qudeisat M. Spatial and temporal carrier fringe pattern demodulation using the one-dimensional continuous wavelet transform: Recent progress,challenges, and suggested developments. Opt. Las. Eng. 2009; 47: 1348–1361.
[26] Liu H, Cartwright AN and Basaran C. Sensitivity improvement in phase-shifted moiré interferometry using 1-D continuous wavelet transform image processing. Opt. Eng. 2003; 42(9): 2646–2652.
[27] Pedraza-Ortega JC, Gorrostieta-Hurtado E, Delgado-Rosas M, Canchola-Magdaleno SL, Ramos-Arreguin JM, Aceves-Fernandez MA and Sotomayor-Olmedo A. A 3D Sensor Based on a Profilometrical Approach. Sensors 2009; 9: 10326–10340.
[28] Dursun A, Özder S and Ecevit FN. Continuous wavelet transform analysis of projected fringe patterns. Meas. Sci. Technol. 2004. 15: 1768–1772.
[29] Forte M. 3D Archaeology: New Perspectives and Challenges The Example of Catalhoyuk. J. E. Mediterr. Archaeol. Herit. Stud. 2014; 2: 1–21 (2014).
[30] Lawing AM and Polly PD. Geometric Morphometrics: Recent Applications to the Study of Evolution and Development. J. Zoo. 2009; 280: 1–7.